Journal of Applied Fluid Mechanics, Vol. 15, No. 6, pp. 1635-1648, 2022.
Available online at www.jafmonline.net, ISSN 1735-3572, EISSN 1735-3645.
https://doi.org/10.47176/jafm.15.06.1163

Novel Induction Blade Design for Horizontal Axis Wind Turbines to Improve Starting Phase: CFD and Testing Analysis

C. Casillas Farfán[1], G. Solorio Díaz[1†] V. López Garza[1], S. Galván González[1] and K. Figueroa[2]

[1] *Faculty of Mechanical Engineering, Universidad Michoacana, Morelia, Michoacan, México*
[2] *Faculty of Physical and Mathematical Sciences, Universidad Michoacana, Morelia, Michoacan, México*

†*Corresponding Author Email: gildardo.solorio@umich.mx*

(Received March 7, 2022; accepted June 25, 2022)

ABSTRACT

This article introduces a novel Induction Blade (IB) prototype modeled by Blade Element Momentum (BEM) theory, which develops higher torque during the starting phase for Horizontal Axis Wind Turbines (HAWT), especially for micro-turbines. The IB is composed of two parallel blades joined at their tips and roots, forming a distinctive hole in the space between the blades that generates a Venturi effect as air passes through. This phenomenon in the IB hole together with the extra lift generated by the area of the second blade produce extra valuable torque during the starting phase. We used Computational Fluid Dynamics (CFD) analysis to evaluate the aerodynamic properties of this design compared with a traditional blade design of the same radius. The IB and traditional prototypes were built (50W, diameter 0.62m, λ=9 and at speed rated 8m/s) by additive manufacturing in a 3D printer and their aerodynamic behaviors tested in a small wind tunnel (square section 0.7m x 0.7m). Our results using CFD analysis show that this novel IB produces up to 65% extra torque without losing output power for low wind velocity (5-8 m/s). IMPI (Mexican Institute of Industrial Protection) protects this prototype shape.

Keywords Torque analysis; Computational Fluid Dynamics; Wind tunnel test; BEM Theory; 3D printing; Prototype; Micro-turbines.

NOMENCLATURE

A_d	turbine swept area
a	axial induction factor
a'	radial induction factor
B_1	blade number 1 in Induction Blade
B_2	blade number 2 in Induction Blade
C_l	airfoil lift coefficient
C_d	airfoil drag coefficient
C_p	power coefficient
c	chord
I_{cp}	integral chord pitch
l_1	blade length of B_1
l_2	blade length of B_2
N	blade number
n	sections number in blade analysis
P	output power
R	blade radius
Re	Reynolds number
r_i	positional radius of i-th blade section
T	aerodynamic torque
Ts	starting torque
W	relative wind speed
U_s	cut-in velocity
U_c	incident velocity
U_∞	wind stream velocity
Ω	rated angular velocity
α	airfoil angle of attack
γ	IB hole flow direction
ϕ	twist angle section
λ	ratio between velocities
μ_i	ratio between r_i / R
ρ	density of air
ψ	induction Blade angle

1. INTRODUCTION

Today there is a growing trend towards renewable energy, including wind power, due to the global commitment to reduce the use of fossil fuels. The small wind world report (Pitteloud & Gsänger, 2017) forecasts a minimum growth of 12% per year in Low-Capacity Wind Turbines (LCWT). The European Norm IEC-61400-2 of 2006 defines LCWT as having less than 7m^2 the swept area with output power P<1KW.

Many sectors of the population (houses, buildings, etc.) could reduce their electricity consumption using LCWT. However, they must be inexpensive, reliable, and almost maintenance-free (Wright & Wood, 2004). Furthermore, they must be located in places with favorable wind conditions (usually, speed ranges 5-8 m/s according to IEC61400-2 norm) to work optimally and therefore be considered for use. However, conditions adverse to LCWT use (no prolonged gusts of wind, no prevailing wind direction, turbulent winds due to obstacles like mountains, trees, etc.) exist in many places.

On the other hand, for high-capacity power turbines used in large wind farms, the investment cost in auxiliary equipment is feasible and recoverable because it maximizes operations. Furthermore, this auxiliary equipment orients the blades toward the best wind direction for start-up when minimum wind conditions exist, thereby extracting significant power at nominal speed. However, use of this type of equipment is not economically justified for LCWT or micro-turbines.

In LCWT, operational deficiencies exist without such auxiliary equipment, and operations depend exclusively on aerodynamic attributes. These attributes are especially important during the self-starting phase, the crucial stage of extracting power at lower wind velocity, called cut-in velocity U_s. Note that, for LCWT, starting is an inherent problem since reduced radius R of the rotor (blade length) results in reduced starting torque T_s . In (Clausen & Wood, 1999), the authors approximated this relationship by $T_s \sim R^3$ (for geometrically similar blades of constant density operating at the same tip speed ratio). Additionally, the starting phase becomes more complex because of the low Reynolds number (low wind speed), high angles of attack, and small size rotors (Clausen & Wood, 2000).

Since the main problem in LCWT is efficiency during the starting phase, this article proposes a new design for a wind turbine blade that enhances its torque properties in the starting phase without losing maximum output power.

Given the importance of the starting process, the phenomenon should be explained in detail. A turbine starts to rotate when the aerodynamic torque developed by the blade shape is higher than resistive torque. Therefore, the blade shape generates two forces under the influence of incident wind: lift and drag. The lift must be greater than the drag to initiate rotation. The resultant vector of combined forces acts on the pressure center in each aerodynamic section in the blade (n sections). Each section has an airfoil located at a distance r_i to the center of the rotor, for $0 < i \leq n$. Each section is responsible for a small torque contribution and total starting torque is the sum of these torques times the number of blades N. It is crucial to design an airfoil with a maximum glide ratio (C_l/C_d) related to the Reynolds number (Re), where C_l and C_d are the coefficients of lift and drag, respectively. Some authors have studied the phenomenon (Vardar & Alibas, 2008), specifically, the recommended four digits NACA's airfoil family for an LCWT. (Singh & Ahmed, 2013; Singh *et al.* 2012) designed airfoils for low Reynolds applications to improve the starting phase. Also, (Shen *et al.* 2015) proposed an algorithm to predict the best aerodynamics characteristics for the starting phase using NACA´s family airfoils.

In (Wood 2001), the author proposed calculating the aerodynamic torque T_s during the starting phase as

$$T_s = \frac{1}{2} N \rho U_c^2 R^3 I_{cp} \tag{1}$$

Where U_c is the incident wind, ρ is the density of air kg/m^3, R is the blade radius and I_{cp} is the integral chord pitch that considers the blade's total inertia moment. In (Wood 2001) claimed that these parameters are not determinants to predict the starting behavior of a turbine; however, they give a hint about the factors that modify it. The starting phase ends when the turbine reaches a constant increment of the angular velocity Ω, 30% of the design angular velocity, $\frac{d\Omega}{dt} > 1$. Unfortunately, few articles focus on analyzing the starting process, and most of them adjust the blade's parameters (chord c, the angle attack α, and the airfoil type) to improve the starting torque, see (Clausen & Wood, 2000; Wood 2001).

(Mayer *et al.* 2001) presented the starting phase of a 5 KW LCWT, D=5m, average wind velocity U_∞ =10 m/s, N=2. Its methodology changed the pitch control angle system from 0° to 35°. They observed the angular speed and torque behavior during the starting phase and concluded that a pitch angle of 20° increased the angular velocity and the aerodynamic torque. The authors claimed this mechanism is unusual in LCWT since a pitch control system is expensive and not amortizable.

(Wright & Wood, 2004) presented a comparison of the evolution of torque during the starting phase comparing BEM theory calculations and actual data from a turbine operating on-site. The authors explained that the difference between actual values and theoretical was due to simplifications in calculating lift and drag coefficients with a high attack angle and a low Reynolds number. They proposed a methodology to reduce the difference between these values, claiming that the starting phase is usually not of concern to designers, who focus on maximum power instead of efficient starting performance.

On the other hand, (Karthikeyan *et al.* 2015) showed a quantitative analysis of design parameters of wind turbines using aerodynamic airfoils. The authors claimed it is too complex to optimize all variables for

starting-phase performance (decreasing the starting time, the idyllic period, and the cut-in velocity) and for rated power simultaneously, because these phases operate under different aerodynamic conditions. The authors analyzed some designs with different aerodynamic airfoils and concluded that the principal contribution to starting torque is near the blade root zone, which also had been stated by (Wright & Wood 2004). The blade root zone (a third part of the long blade) gives near 50~70% of the total starting torque.

These authors agree that optimization of starting torque requires improving aerodynamic blade properties to increase torque and reduce starting time. Unfortunately, their optimizations have not increased starting torque by more than 7 percent; nevertheless, these authors have done laborious optimization processes, and in some cases have resulted in less rated power. The need to start turbines efficiently has motivated designers to propose new blades designed to improve the starting phase.

This article introduces a novel Induction Blade prototype. This invention is for HAWT, especially LCWT and micro-turbines, to develop higher torque during the starting phase without reducing the rated output power. The prototype shape presented is protected by IMPI (Mexican Institute of Industrial Protection).

The IB's aerodynamic design is based on BEM theory which combines moment conservation equations and Blade Element Theory to calculate turbine aerodynamic performance (Schaffarczyk, 2014). BEM theory assumes ideal air conditions (axial incompressible steady flow); control volumes for analysis are formed by concentric rings with uniform properties; losses due to turbulence, energy dissipation, or rotational wake are not quantified.

(EL-Okda 2015) proposed a compilation of multiple optimization theories and comparison between them, including BEM theory, to determine the relative advantages. The authors compared the Schmitz and Burthom methods, mentioning that greater twist angles are required in the root zone to produce sufficient starting torque, properties that closely coincide with results of the BEM theory.

2. Induction Blade. Concept and Modeling

Induction Blade (IB) is a body composed of two blades: the frontal (primary blade) B_1 and the secondary blade B_2 (see Fig. 1). Moreover, B_2 is a replica of the first aerodynamic sections of B_1 trimmed to a specific length. Likewise, the B_2's root zone is joined to the first aerodynamic sections of the primary blade. It is essential to notice that B_1's aerodynamic design is modelled using BEM Theory in a traditional blade process.

Furthermore, positions of B_1 and B_2 are closely related. Let D_x, D_y, and D_z be the position coordinates on the x, y, z-axis of the design plane of B_2 regarding B_1's leading edge in the first aerodynamic section. Additionally, the vertical position of B_1 and the inclination of B_2 form an internal angle ψ (induction angle). Let l_1 and l_2 be the length of B_1 and B_2 respectively (see Fig. 1). Finally, γ is in the counter-clock direction, and it is the angle to avoid that B_2 will be parallel to B_1 on the z-axis.

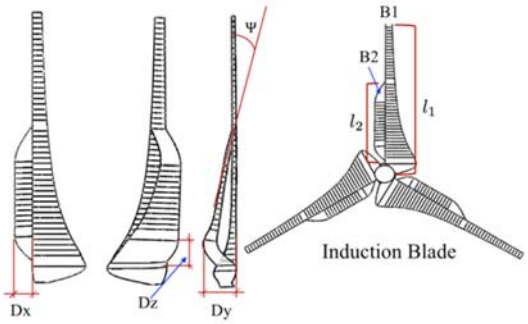

Fig. 1. Views of HAWT with Induction Blade.

IB design was conceived to have a larger contact area and thus increase the lift force. Preliminary studies of IB show an increase in lift force and thus a higher torque. There are two factors contributing to this increased lift force: the presence of the second blade, and the wind's induction effect generated in the space (hole) between the blades.

Thus, when the wind passes through the induction hole it creates the Venturi effect (see Fig. 2). An incompressible fluid's velocity must increase as it passes through a constriction in accord with the principle of mass continuity, while its static pressure must decrease in accord with the principle of conservation of mechanical energy (Bernoulli's principle).

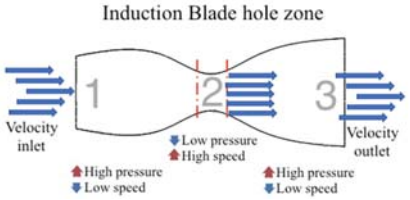

Fig. 2. Venturi effect on the induction hole.

The higher velocity in the hole between the blades produces a lower pressure which means a higher lift force. The lift force produced by both blades (B_1 and B_2) generates the total torque. The wind induction produced in the hole between blades inspired the name of *Induction Blade*. Fig. 15(h) shows the Venturi wind effect when it passes through the IB (zone in blue is the hole in the blade).

2.1 Design of the 1st Blade

The BEM theory discretizes the blade in n aerodynamic sections (See Fig. 3 in which gray zone is a section). In our design, n=50 provides high precision for aerodynamic blade shape. For each section, lift and drag coefficients were calculated (C_l,

C_d); designers must propose the airfoil angle attack and Reynolds number (*Re*) is calculated. In our study, Q-Blade Software was used to find both coefficients for a NACA airfoil 4412.

Otherwise, the Power Coefficient (C_p) describes the overall performance of a wind turbine, which is the ratio between actual output power and power available on the wind stream.

$$C_p = \frac{P}{\frac{1}{2}\rho U_\infty^3 A_d} = 4a(1-a)^2 \quad (2)$$

Where U_∞ is the wind stream velocity for rated power, $A_d = \pi R^2$ is the rotor's swept area (m^2), the ideal value known as the Betz limit is C_p=0.59, taken as the preliminary value to design a turbine. From Eq. 2, it is possible to calculate A_d and R, which represent the swept area needed and the radius of the turbine.

A significant value to consider is tip speed ratio λ (dimensionless), which is the ratio between the angular velocity and the mean velocity of the fluid; usually λ takes values between 6 and 9. It is $\lambda = \Omega r_i / U_\infty$, where Ω is the rated angular velocity in rad/s.

Since one blade turbine has *n* sections, each must calculate its aerodynamic properties (see Fig. 3, source (Tony Burton David Sharpe & Bossanyi, 2001). First, the value of radial induction factor for each section *i* is calculated as follow:

$$a_i' = \frac{a(1-a)}{\lambda_i^2} \quad (3)$$

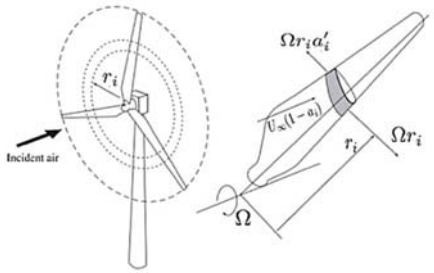

Fig. 3. Blade discretized in sections.

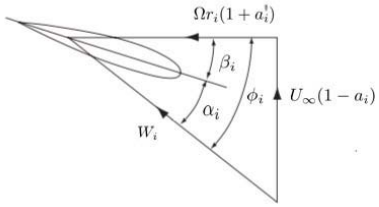

Fig. 4. Triangle velocity for the *i*-th section.

Where λ_i is related to the positional radius r_i, and a is the axial induction factor, which is the reduction of the velocity of the wind in the free stream and the contact with the turbine; typically, a=1/3, a theoretical value where the power coefficient is maximized.

The velocity triangle must be calculated in every section to know the aerodynamic properties (see Fig. 4, source (Tony Burton David Sharpe & Bossanyi, 2001). The wind velocity U_∞ and the angular velocity Ω form the velocity triangle. The relative wind speed W_i is the velocity resultant over each airfoil *i*. The equation to calculate W_i is

$$W_i = \sqrt{(U_\infty^2(1-a)^2) + (\Omega^2 r_i^2(1-a_i')^2)} \quad (4)$$

W_i and the plane of the rotor form the *twist angle* ϕ_i as follow:

$$\sin\phi_i = \frac{U_\infty(1-a)}{W_i} \quad (5)$$

Finally, the chord c_i of each airfoil is:

$$c_i = \frac{4\lambda\mu^2 a_i' U_\infty 2\pi r_i}{W_i C_l N} \quad (6)$$

Where μ is the ratio between r_i/R. The distance r_i defines each section to the rotation center, chord length c_i, and twist angle ϕ_i. Fig. 5 shows the distribution of each chord per section along with the radius blade of B_1.

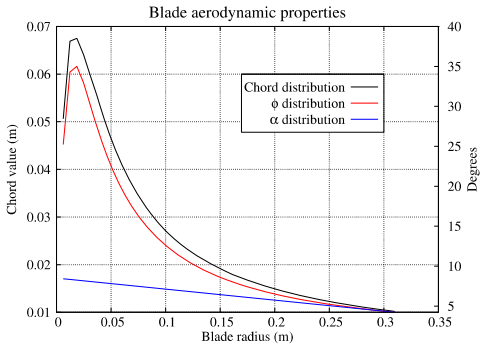

Fig. 5. Size of each chord along the radius for B_1.

(Khalil *et al.* 2018) proposed a method to optimize and find the radial a_i' and axial a induction coefficients, allowing them to find the best configuration to maximize output power. The span-wise blade tends to be thinner in the root zone, while the tip direction remains almost without change. This optimization is not attractive for our design because the authors focused on maximizing the output power and not on improving the starting phase. Therefore, IB design must have a tradeoff between an efficient starting performance and the output power.

2.2 Design of the 2nd Blade

In section 3.1, the design parameters were considered only for the main blade (B_1) but not for the second blade (B_2).

The second blade has the same aerodynamic properties as the primary blade, under the presumption that B_2 has a direct incidence of the

wind stream and, consequently, similar aerodynamic behavior. Therefore, modifying excessively the aerodynamic characteristics of B_2 could lead to synchronic aerodynamic problems. It means that B_2 must behave aerodynamically similar to B_1 and contribute to the general performance.

The aerodynamic shape of the induction blade B_2 is then equal to the primary blade, considering only the aerodynamic sections corresponding to a length equal to $l_2 \leq \frac{1}{2} l_1$ since just those sections near to the blade's root zone contribute to the starting torque as claimed by (Wright and Wood 2004).

3. METHODOLOGY AND NUMERICAL SIMULATION

The software *Fluent* is a powerful computational tool for analyzing dynamic fluid phenomena and has proven reliable in solving fluid-solid-interaction problems involving geometries with complex shapes. In addition, some authors have used *Fluent* software to evaluate aerodynamic behavior in their designs (Hsiao *et al.* 2013; Tahani and Moradi 2016; Amiri *et al.* 2019; Ramarajan and Jayavel 2022).

Our methodology for steady-state (speed of rotation zero) torque analysis was as follow:

1. A traditional 50W rotor was designed using BEM theory to study theoretical aerodynamic properties. This turbine will be called *the reference model* (50W-RM).
2. The 50W-RM was manufactured using a 3D printer and tested in a small wind tunnel to get the actual values of starting torque. At the same time, an initial CFD setup was proposed.
3. The torque values obtained at point 2 were used as a reference to validate the CFD model of the 50W-RM. The boundary conditions, turbulence model, and general setup were defined to solve the fluid-body interaction.
4. To study an IB as a new design with no information about its fluid behavior and similar features to traditional turbines, we use the 50W-RM *Fluent* setup as a reference. It means this is the preliminary CFD study for IB design.
5. After the numerical analysis using CFD with an IB and confirming its improvement in starting torque, an IB prototype was manufactured in the same way with a 3D printer and tested in the same wind tunnel. This step was to validate the IB aerodynamic behavior. Moreover, we could modify the parameters of the coordinates to get an IB's improved CFD-validated model.

3.1 Reference Model Design (50W-RM)

The square section of the wind tunnel available was 0.7x0.7m; for this reason, the reference model designed (50W-RM) has a length of 0.31m, an output power of 50 Watts at speed rated 8m/s and λ=9. The prototype rotors were placed outside the wind tunnel to avoid air contraction due to the walls, as this could alter the wind tunnel velocity (Abdelgalil *et al.* 2019; Ryi *et al*. 2014). Outside the tunnel, the wind turbine prototypes were placed one meter apart since, at this distance, there was no considerable variation in wind speed regarding the tunnel outlet, see figure 9. Additionally, calculating and evaluating on MATLAB the equations related to BEM theory of section 3.1, the results were: cloud coordinates points with the aerodynamic profiles, chord characteristics, and twisted angle along the radius of the blade for each section. After that, the cloud points describing each aerodynamic section were used to create the virtual model and finally get the 3D design geometry, which was done quickly with *SpaceClaim* software. Then, the solid model of 50W-RM was sliced in *Simplify 3D* software and printed by layer addition technology, better known as 3D printing. The material used was PETG.

A cup anemometer calibrated the velocity stream of the wind tunnel at the center of the turbine's hub. During the experiment, a torque meter measured the torque triggered for 50W-RM in a range of wind velocities U_∞={3,4,5,6,7,8}m/s. The starting torque values measured were used to validate the precision of the CFD model (see section 4.3).

These results were similar between both models for steady-state: CFD and the 3D printed prototype of 50W-RM tested. Therefore, the CFD results are valid to evaluate the aerodynamic performance for the prototypes used. Furthermore, the CFD-validated model is acceptable for the boundary conditions, turbulence model, and *Fluent* setup. Notice that the difference between testing and numerical solutions was because we reported the lower values from the instrument during measurement. Therefore, this criterion is consistent for all measurements.

3.2 Induction Blade Design

In the first numerical analysis, the extra starting torque that the IB design triggered was around 30% for each velocity tested in comparison with the 50W-RM. In contrast, the improvement was around 20% in the wind tunnel test. However, this first proposal had a high blade inertia (almost 50% extra).

The proposed analysis for IB design parameters was a combination process evaluating aerodynamic performance, starting torque behavior, and blade inertia. Our goal was a higher starting torque with lower blade inertia. The parameters of the position of B_2 regarding B_1 obtained experimentally that achieved our goal (only +35% of increment on blade inertia) were: D_x=0.019m, D_y=0.02m, D_z=0.02m, ψ=8°, γ=8° and l_2=0.1m. This IB configuration was used during our experimental comparison (described in section 5). Naturally, these parameters modify the blade B_2's exposure to the wind stream and thus the aerodynamic behavior. As D_x and D_y become high, the manufacturing process can be complex, and even worse, the Venturi effect in the induction hole can be affected, reducing the extra torque.

In this paper, we only discuss the aerodynamic effects for our IB design compared with a traditional turbine, considering the starting torque produced and the rated output power.

The final IB design was also manufactured using a 3D printer and tested in the same wind tunnel. The starting torque values were similar, between 2 to 9%, comparing the IB and CFD models. Therefore, the difference is similar to values obtained for the validation process of 50W-RM analysis and can be considered a valid CFD model to study IB behavior. Again, the difference was due to average values taken during measurement.

3.3 Computational Domain, Boundary Conditions and *Fluent* Set-up

The computational domain for numerical simulation is the virtual space geometry used to replicate the conditions of the experiment to be analyzed. For example, in the case of turbines, most authors who develop computational fluid dynamics analysis propose two domains: an inner and an outer cylinder according to Multiple Reference Frame (MRF) technique (Amiri *et al.* 2019) (see the frontal view in Fig. 6 and the isometric view in Fig. 7). The interaction between fluid and turbine body is calculated inside the inner domain, while the outer one mainly simulates the incident wind stream properties and the confined wind space.

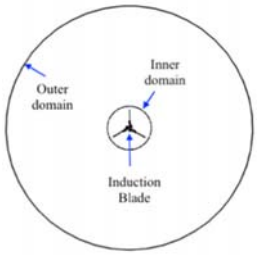

Fig. 6. Frontal view of computational domain used.

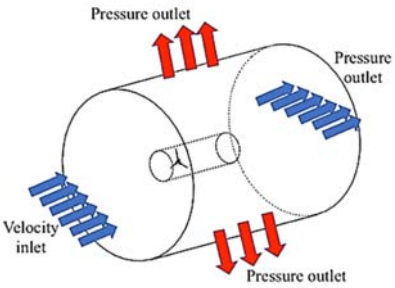

Fig. 7. Isometric view of computational domain used.

The boundary conditions used were inlet velocity (at the front face), outlet pressure on the outer domain (rear face and lateral walls) set at zero gauge-pressure, and wall condition for the rotor silhouette. The isometric view of Fig. 7 shows the different boundaries used.

The geometric dimension of the computational domain for this study is: the inner cylinder has a length of 4 x D_{in}, where D_{in} is its diameter and relates to turbine diameter (2*R*). In this case, D_{in} was 0.62m. On the other hand, the outer cylinder has a length of 10 x D_{in}, and the diameter in this cylinder is D_{out}=8 x D_{in}. The turbine's body is inside the inner cylinder at 2 x D_{in} length from the circular face. Therefore, the inner cylinder is inside the outer at 3 x D_{in} length. This design is similar to the one proposed by (Hsu *et al.* 2021).

The computational domain was replicated in the most exact way using the meshing technique. The mesh used comprises tetrahedral elements created by a Patch Independent Meshing Algorithm for the inner cylinder and Patch Conforming Meshing Algorithm for the outer one.

Both algorithms have the benefit of adapting to geometries in complex shapes like blade turbines and perform refined meshing with high precision. Moreover, the height of the first layer of the mesh above the blade area (0.0008m) was calculated; this is necessary to obtain a suitable value of Y+. In addition, a refinement was applied to all the blade faces, and the leading and trailing edge zones were controlled by local control of the minimum element size at 0.0005 m, while the average element size was 0.0015 m. On the other hand, the transition of the size of the elements was controlled, that is, the growth rate for subsequent layers, whose value was 1.2. Local refinements result in a reduction in the domain's elements.

Additionally, these algorithms considerably reduce the time of the meshing process. The mesh independence obtained was achieved at 6.8 million elements, with a maximum skewness of 0.86. Fig. 8 presents a meshed IB.

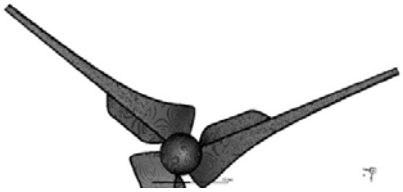

Fig. 8. Induction-blade meshed with tetrahedral cells.

The turbulence model used was k-ω *SST* since it has reported good agreement between measurements and numerical calculations (Eltayesh *et al.* 2021). For this model, the Y^+ value is sensitive to the wall distance. For our study, the average Y^+ was similar to the velocity magnitude of every analysis; it is $Y^+ \sim Uc$. The local minimum size and the growth rate values were combined to analyze the results regarding the value of Y+. With this, it was found that there were negligible variations of 2 or 3% even when Y+ was reduced to half.

The *Fluent* setup was determined mainly by the stability of the residuals solution, reaching values of $1x10^{-5}$ corresponding to continuity, velocities, and turbulence equations of the model. Our *Fluent* setup considered the following: incompressible fluid, a Coupled-Scheme for the pressure-velocity solution, and spatial discretization with the Green-Gauss cell-

based method. In addition, a second-order discretization scheme was used to solve the properties of the fluid movement and a hybrid initialization.

The Hardware used in this analysis was a computer with 16GB RAM and dual-core i7 processors 8th gen.

4. RESULTS AND DISCUSSION

Once the 50W-RM Model analysis was complete (theoretical, tested, and CFD-validated model), the same methodology was used to analyze the IB turbine. The *Fluent* setup used was identical, and the manufacturing and testing process performed with the same techniques. Fig. 9 shows the IB turbine and wind tunnel. In Fig. 10, IB is on a torque meter obtaining torque data. It is essential to mention that experiments for both models were under the same conditions (for CFD and wind tunnel tests).

Fig. 9. Bench test of the Induction Blade.

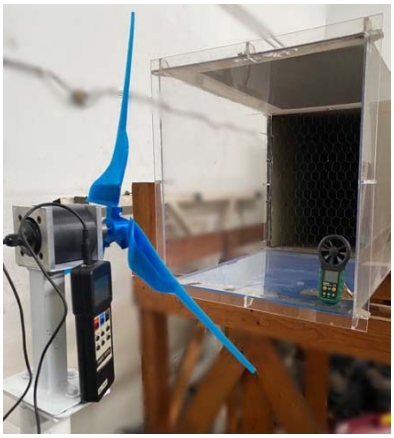

Fig. 10. Calibration test of the Induction-Blade on the wind tunnel.

The starting process involves two different analyses. One, in steady-state to evaluate instantaneous torque produced by incident wind. The second, an analysis using MRF to assess evolution of torque during the first blade turns until nominal speed is reached.

4.1 Torque Analysis

Figure 11 shows the torque performance: 50W-RM (lines in red), and IB (lines in blue), the *x*-axis the wind mean velocity used (m/s), and the *y*-axis the starting torque (Nm) produced by incident wind. The CFD results for both models (dash lines) show that IB has a higher performance than 50W-RM in the steady-state analysis. Notice that the IB torque obtained with CFD had an increase from 65% (at 3m/s) to 68% (at 8m/s) for the wind velocity used. CFD results for both models were validated using the manufactured models (solid lines). Line in green is the theoretical 50W-RM calculated using BEM theory (Eq. 1). Notice the difference between the BEM theory theoretical model plotline (green) against 50W-RM manufactured (solid line in red) due to the lift coefficient C_l in the term I_{cp} (Eq. 1). C_l is complex to compute during the starting phase because the Reynolds number is low (Re<200,000) and the airfoil angle of attack is high at first turns but decreases when the turbine accelerates. In addition, it becomes challenging to predict this coefficient under starting conditions due to the separation of the boundary layer. On the other hand, notice that the CFD model has a similar behavior against manufactured prototypes.

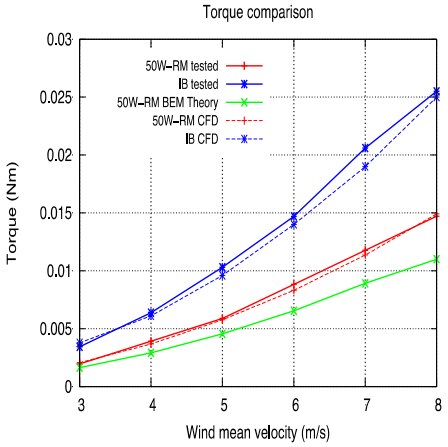

Fig. 11. Performance comparison between 50W-RM and the IB proposed using CFD.

The exposure of B_2 to the wind mainstream increases its lift. That means B_2 generates its lift in the same direction as B_1's lift, contributing to the thrust, and consequently, B_2 provides extra torque to the IB rotor. As the exposed area or length of B_2 increases, the lift and drag forces and the moment of inertia tend to increase.

With the presented configuration of B_1 and B_2, the B_2 blade contributes up to 60% of the lift of the IB. The key is to keep B_2 exposed to the mainstream by D_x, D_y, D_z, and l_2, and that air can be ducted through the induction hole. The limiting case is when B_2 is parallel to B_1 when D_x=0; it is precisely behind B_1, and B_2 is not exposed to the mainstream. In this scenario, no lift is produced in B_2, and therefore the extra torque tends to zero.

Additionally, to compare the fluid-blade interaction for both models, we calculated Thrust (wind force over the rotor) and average static pressure over the surface of the turbine. Table 1 shows these computed aerodynamic properties. In the Thrust column for both models, when wind velocity is 3 m/s IB has 25.63% higher than 50W-RM; for 4-8 m/s, IB increases 25.66%, 25.78%, 25.47%, 25.81%, and 25.83%, respectively. Something important to note is that the extra torque produced by IB is due to the extra lift generated by B_2 in consequence of the additional thrust force over it. Notice that IB with this velocity range has a slight Thrust increase, which allows us to confirm that in operation with a higher Reynolds number, the starting torque of the IB is not affected by greater turbulence.

The average calculated pressure is related to the interaction between fluid and turbine around the blades. Comparing the pressure value for IB against 50W-RM at the same wind velocity, the value for IB will be consistently higher than 50W-RM because there is a larger contact area that decreases the velocity of the fluid. In this way, the fluid leaves the 50W-RM at higher velocities than the IB body and compensates for the pressure drop (see figures 14 and 16).

The analysis until now corresponds only to the rotor at steady-state. However, as a rotor begins to rotate, the velocity triangles are modified, resulting in a change in the rotor's angular velocity, which can be solved using the MRF technique.

Figure 12(a) shows the torque performance against shaft rotational speed for a rotating reference frame analysis comparing 50W-RM against IB for incident wind velocities between 5-8 m/s. Notice that IB kept a higher developed torque during the beginning of the starting phase and tends to be similar in the curve's peak for every velocity tested. Solid lines represent the IB performance, and the dash ones are for 50W-RM. The relevant fact is that the improvement in torque is observed immediately as the turbine leaves the rest state. This proposal makes it possible to start turning at a lower wind velocity. Notice that for rotational speed less than 100 the IB's torque is higher than 50W-RM.

Additionally, in Fig. 12(b), it is possible to see that the maximum output power is almost the same for IB (lines in blue) with respect to 50W-RM (dash lines in red). Notice that even during the first rotational speeds, the power of IB is slightly higher than 50W-RM and tends to be similar at curve peak. Then, when the maximum output power is reached in both turbines and the shaft rotational speed increases, their output power tends to decrease. Thus, there is more power loss as Ω and wind velocity increase, confirming that IB is designed for low wind speeds. Therefore, a generator matched to maximum output power at a specific rotational speed will limit the acceleration of the rotor, avoiding the power decreases.

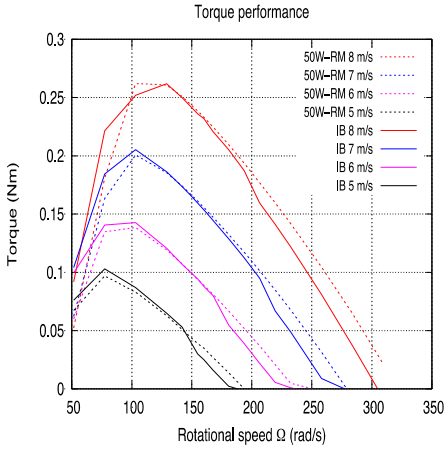

(a) Torque performance with U_c velocities.

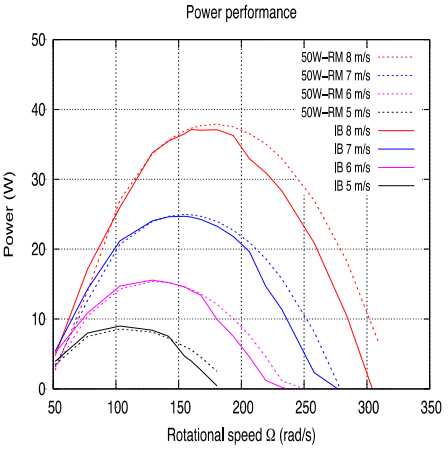

(b) Power performance with U_c velocities.

Fig. 12. Comparison performance for 50W-RM and IB using CFD. analysis.

Table 1. Aerodynamical behavior obtained over the rotors triggered by the incident wind.

	50W-RM Model			Induction Blade			
Incident velocity (m/s)	Torque (Nm)	Thrust (N)	Average pressure (Pa)	Torque (Nm)	Thrust (N)	Average pressure (Pa)	% Torque Increase
3	0.002069	0.1705	-3.56	0.0037	0.2142	-3.37	78.83 %
4	0.003680	0.3028	-6.33	0.0061	0.3805	-6.07	65.76%
5	0.005762	0.4724	-9.96	0.0096	0.5942	-9.61	66.60%
6	0.008319	0.6792	-14.51	0.01403	0.8553	-14.07	68.65%
7	0.01137	0.92	-20.02	0.01913	1.162	-19.46	68.24%
8	0.01490	1.20	-26.57	0.025	1.51	-25.8	67.78%

Table 2. Average velocity and pressure values obtained at inlet an outlet planes for 50W-RM.

50W-RM	Inlet plane		Outlet plane		
Incident velocity (m/s)	Average velocity (m/s)	Average pressure (Pa)	Average velocity (m/s)	Average pressure (Pa)	Delta velocity (m/s)
3	2.66	1.20	2.27	-1.75	0.39
4	3.54	2.12	3.019	-3.11	0.521
5	4.43	3.30	3.76	-4.86	0.67
6	5.32	4.73	4.51	-7.02	0.81
7	6.21	6.41	5.26	-9.59	0.95
8	7.10	8.33	6.021	-16.58	1.087

Table 3. Average velocity and pressure values obtained at inlet an outlet planes for IB.

IB	Inlet plane		Outlet plane		
Incident velocity (m/s)	Average velocity (m/s)	Average pressure (Pa)	Average velocity (m/s)	Average pressure (Pa)	Delta velocity (m/s)
3	2.59	1.41	2.185	-1.38	0.405
4	3.45	2.50	2.72	-2.8	0.73
5	4.332	3.89	3.40	-4.43	0.92
6	5.18	5.59	4.08	-6.37	1.1
7	6.04	7.59	4.76	-8.67	1.28
8	6.91	9.40	5.45	-11.31	1.46

4.2 CFD Results

Thrust, static pressure, and torque describe the behavior of wind on the turbine surface, but it does not consider the fluid properties on the incident windstream. To analyze this wind behavior along the winding path (velocity, pressure average, and direction) for both models, we placed imaginary circular planes (inlet and outlet) of D=0.6m and a distance of 0.05m from the body (see Fig. 13) on each side. Tables 2 and 3, 50W-RM and IB, respectively, show average values of the properties in these planes.

Average velocity values obtained over the inlet plane of IB are lower than 50W-RM because of the larger contact area. Also, this reduction in velocity represents an increase in static pressure due to the air mass braked on it. In Table 3, it is possible to notice a similar behavior for each incident velocity.

On the other hand, Table 3 shows the average velocity values obtained for the IB model on the outlet plane after the impact on the rotor, showing a decrease in the average wind mainstream. The IB model has a velocity drop of around 26.90% between both planes, while for 50W-RM, the value is 17.89%, which means IB has better interaction with the fluid. The velocity reduction in the mainstream between planes does not determine that the turbine has efficiently used the energy from the wind; the increase in the torque confirms it.

This analysis over inlet and outlet planes gives an idea of the average properties in the zone that wind tends to pass. Finally, we placed a new imaginary transversal plane to visualize the properties resultant due to interaction between fluid and body, see Fig. 13 (green area). This plane is along the winding path and cuts on a blade on the rotor. Fig. 14 and 16 show the pressure and velocity contours on this plane.

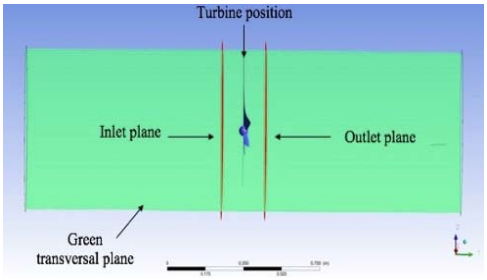

Fig. 13. Planes used to compute and visualize fluids properties.

Moreover, models have a comparison; on the left side is 50W-RM for values of 3-6 m/s, while IB is on the right side with the same wind ranges.

The pressure contour figures (14 and 16) used a filter scale from -70 to 20 Pa to visualize the evolution of average static pressure. Different zones have letters A, B, C, or D. A is the front hub zone, B tip zone, C is the beginning of the induction blade, and D is the rear zone on the turbine.
Comparing the contour pressure of the figures 14(a), 14(c), 14(e), and 14(g) with 14(b), 14(d), 14(f), and 14(h), respectively, an increase in pressure in Zone A exists for IB models, as we claimed, and is due to a larger contact area and reduced air mass that crosses it. In the case of the contours in zones B, C, and D for both models and each velocity, a change in the outlet pressure distribution can be seen; clearly, the figures show zones with lower pressure on IB models. In the C-D zones, the additional reduction in pressure is remarkable because of the B_2 blade, more impressive in Fig. 14(h).

A similar analysis of pressure contours can be made when the air leaves the turbine (see Fig. 15). In this case, we used a circular plane in a tangent position to

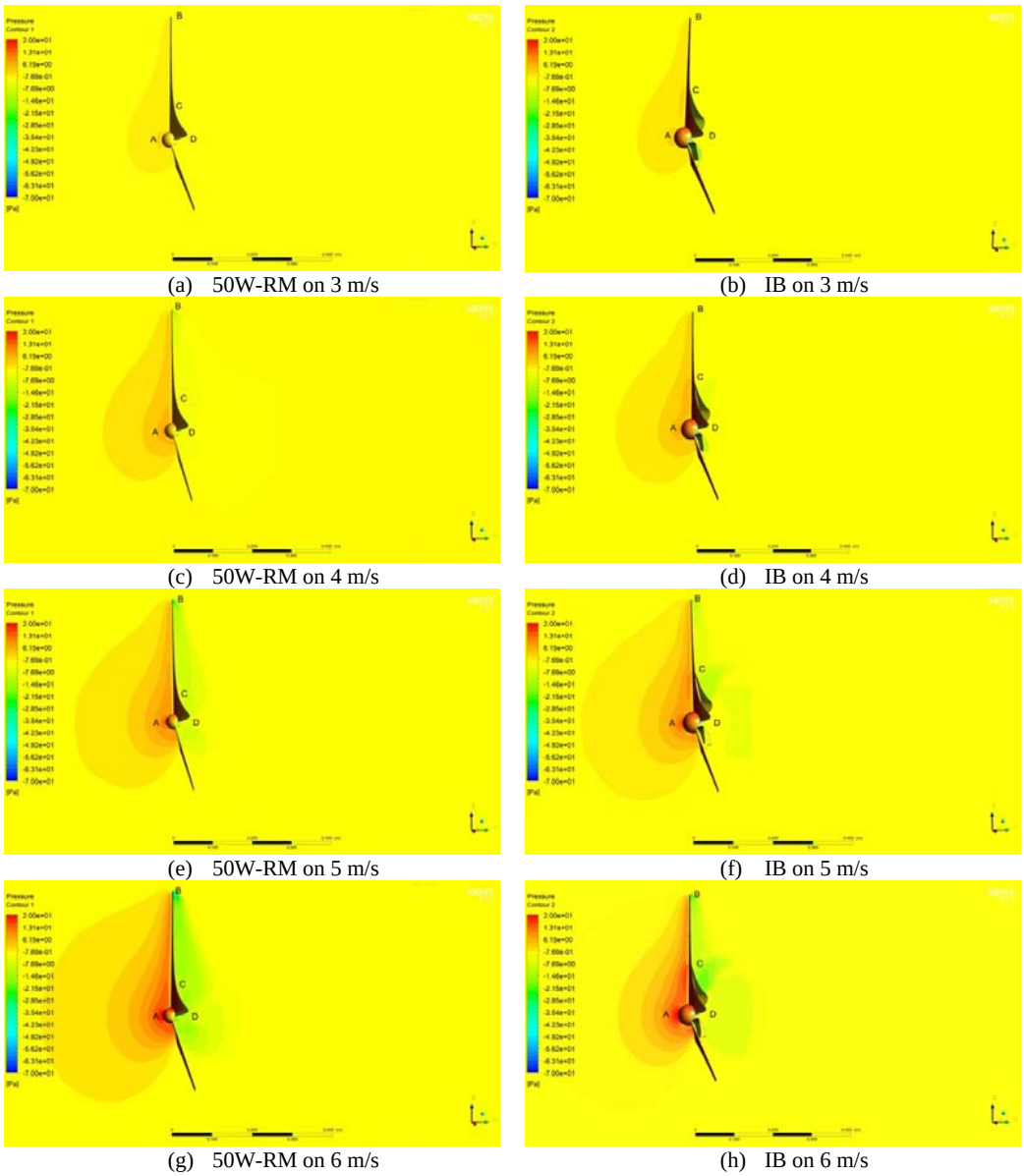

(a) 50W-RM on 3 m/s (b) IB on 3 m/s

(c) 50W-RM on 4 m/s (d) IB on 4 m/s

(e) 50W-RM on 5 m/s (f) IB on 5 m/s

(g) 50W-RM on 6 m/s (h) IB on 6 m/s

Fig. 14. Pressure contour on lateral view (left side 50W-RM, right side IB) with 3m/s (top) to 6m/s (bottom) using CFD analysis at outlet plane.

the turbine's rear face of the blade. Again, Fig. 15 shows on the left side the 50W-RM and on the right the IB, with a direct comparison of wind velocity from 3-6 m/s. Two important zones are observable, zone E around hub and F for the tip.

Note that the pressure dropped for 50W-RM is almost uniform along the blade (the line between E and F labels) for all cases, see figures 15(a), 15(c), 15(e), and 15(g); however, in the case of IB, the higher drop is concentrated in the hole's induction zone (E), see figures 15(b), 15(d), 15(f) and 15(h). These contours show the contraction of fluid in this zone. The interaction between fluid and IB modifies the winding path in the induction zone, which triggers an extra expansion of the air, leading to an impulse over the rotor (which means extra torque). Notice the contour of pressure silhouettes over induction holes in Fig. 15 (near zone E), which are the distinctive feature of IB.

Finally, Fig. 16 shows the direction and magnitude of the wind stream with velocity contour

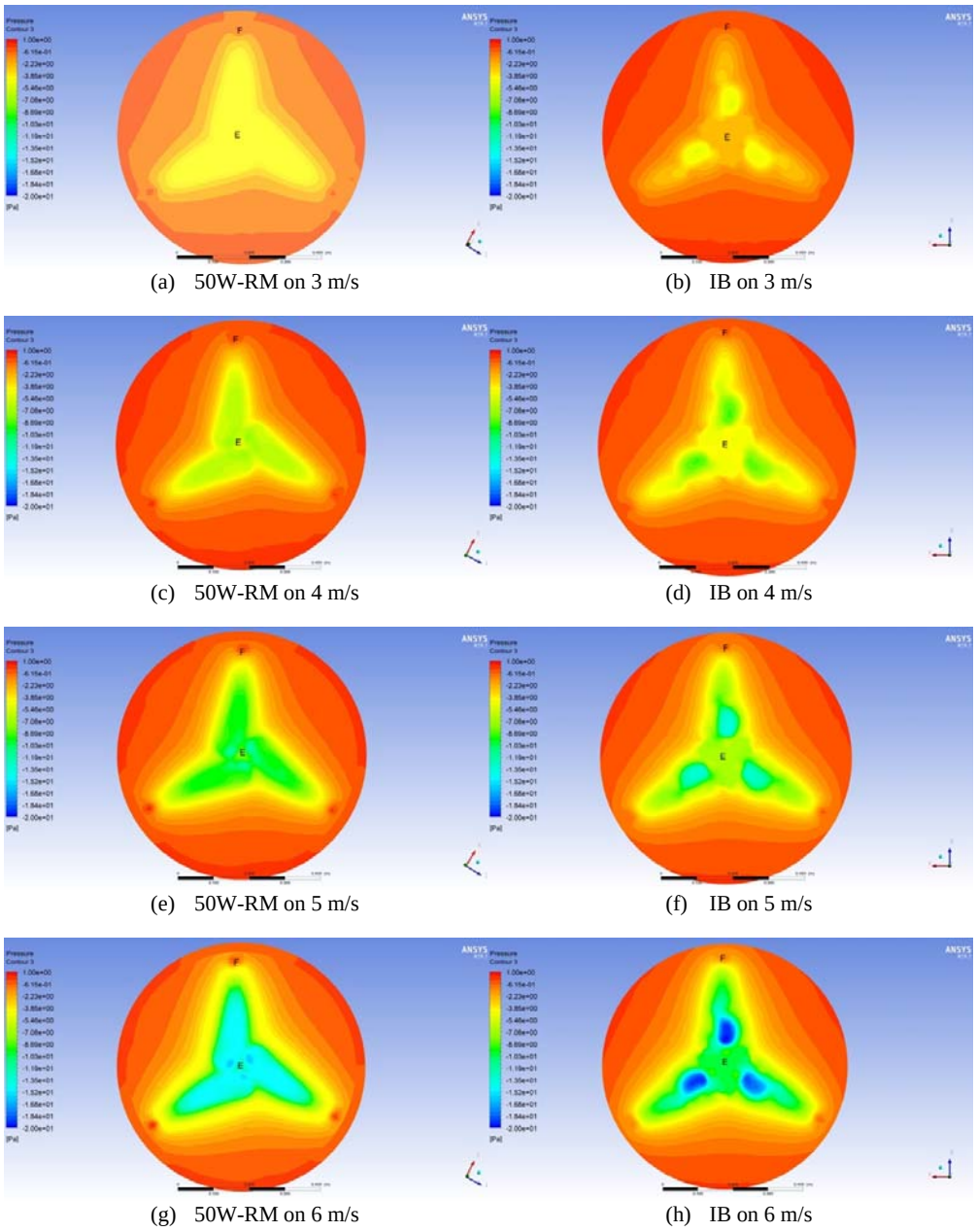

(a) 50W-RM on 3 m/s (b) IB on 3 m/s

(c) 50W-RM on 4 m/s (d) IB on 4 m/s

(e) 50W-RM on 5 m/s (f) IB on 5 m/s

(g) 50W-RM on 6 m/s (h) IB on 6 m/s

Fig. 15. Pressure contour on rear view (left side 50W-RM, right side IB) with 3m/s (top) to 6m/s (bottom) using CFD analysis at outlet plane.

superimposed with vectors towards the *x*-direction. The vectors indicate each section's predominant direction of movement, and the vector lengths were normalized. The scale used for all velocity-contour cases is 10 m/s for higher value and 0 for the minimum. There are two zones studied: one, with the letter G, near the blade's rear zone, and H for recirculation zones. The 50W-RM is on the left column and the right for the IB. Comparing the H zones for 16(a) and 16(b), 16(c) and 16(d), 16(e) and 16(f), and 16(g) and 16(h), note that there are two well-defined recirculation zones because the extra lower pressure behind the IB against 50W-RM. These recirculation zones do not affect the turbine performance because there is an increase in torque.

Zone G tends to be a free zone for the wind stream in the case of 50W-RM, while for IB the velocity in this zone decreases because the wind is stopped by the larger contact area (the induction blade), all cases having the same behavior. Therefore, this reduction in velocity magnitude indicates that the wind stream loses energy in the turbine, and has the advantage of gaining torque.

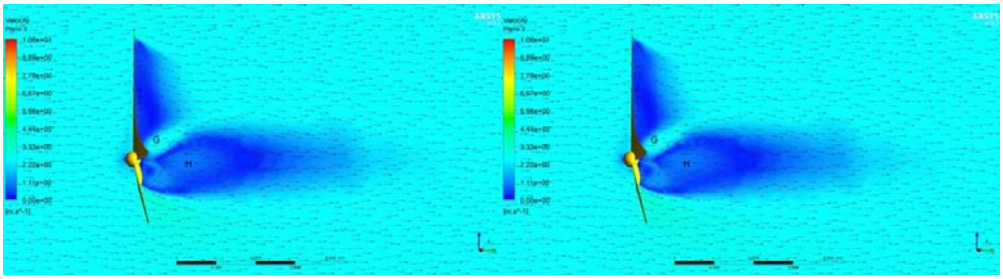

(a) 50W-RM on 3 m/s (b) IB on 3 m/s

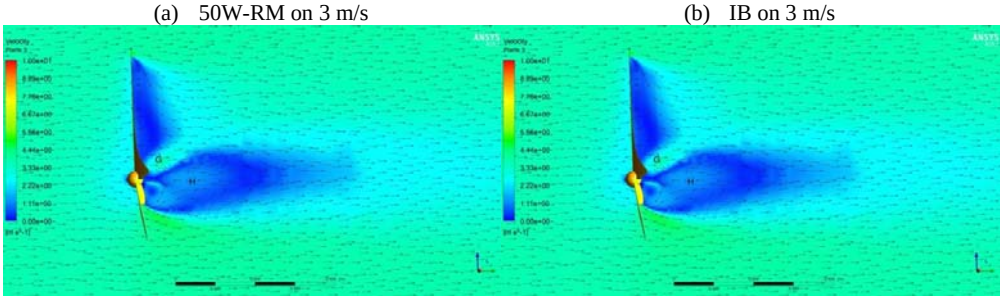

(c) 50W-RM on 4 m/s (d) IB on 4 m/s

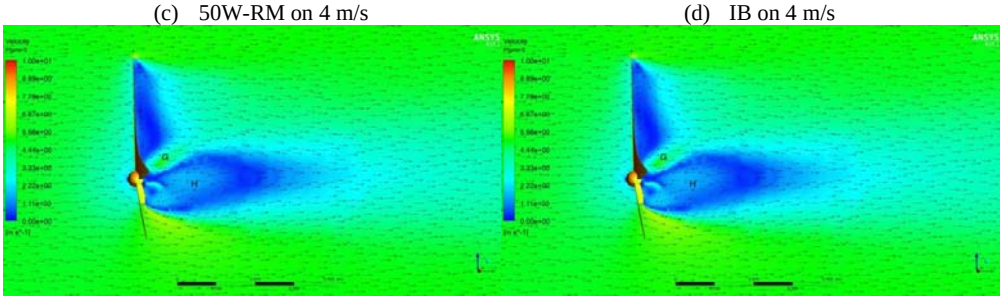

(e) 50W-RM on 5 m/s (f) IB on 5 m/s

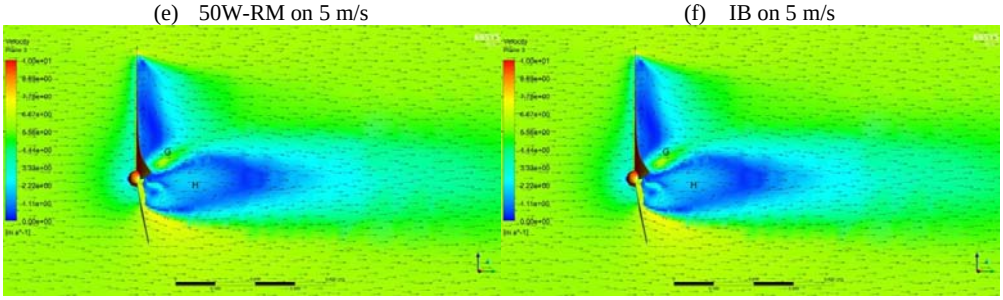

(g) 50W-RM on 6 m/s (h) IB on 6 m/s

Fig. 16. Velocity contour on lateral view (left side 50W-RM, right side IB) with 3m/s (top) to 6m/s (bottom) using CFD analysis at green transversal plane.

5 CONCLUSIONS

This paper proposes a novel aerodynamic design called Induction Blade (IB) for a Horizontal Axis Wind Turbine to develop a higher starting torque than traditional wind turbine blades. IB is composed of two blades, the main blade designed using BEM theory, and the second a copy of the first located strategically behind its leading edge to form an induction hole in the space between the blades.

We validated numerical solution for a traditional turbine starting process with the data obtained from a testing bench. In addition, benchmarking (the CFD setup, boundary conditions, and general software configuration) was used to analyze the IB's aerodynamic behavior. It is possible because both models have similar behavior. The entire analysis described in this article uses BEM theory, CFD numerical simulation, and 3D printed prototypes tested in a wind tunnel.

This study concluded that IB produces a higher starting torque, on average 65% higher for all operation ranges (according to CFD analysis) and 71% higher for tested values in the wind tunnel. The increased torque is due to the lift generated by the second blade and the Venturi effect in the hole formed between blades. Therefore, considering that

IB develops a higher torque, it will start rotating with lower wind velocities.

A cost-benefit analysis will be interesting between IB against a traditional turbine. Any extra cost of manufacturing an IB should amortize due to more time in power production.

An IB design with optimal parameters develops a higher starting torque without losing output power. Our proposal is feasible for use as an alternative design in conditions with low wind velocities (4-6 m/s) and tip speed ratio (λ) less equal to six. Additionally, IB can scale to larger turbines for possible benefits there.

In the future, we are interested in optimizing the blade shape and mechanical stresses while IB is operating.

ACKNOWLEDGEMENTS

The authors gratefully acknowledge the CONACYT for the financial support to Christian E. Casillas Farfán to conduct his graduate studies. We also thank UMSNH for allowing us to use facilities and equipment for developing this work.

REFERENCES

Abdelgalil, E., B. M. Hanna, F. Castellani, A. S. Huzayyin, H. M. El-Batsh, B. Massimiliano and M. Becchetti (2019). Effect of Wind Tunnel Blockage on the Performance of a Horizontal Axis Wind Turbine with Different Blade Number. *MDPI* 12(10), 1988.

Amiri, M., M. Kahrom and A. R. Teymourtash (2019). Aerodynamic Analysis of a Three-Bladed Pivoted Savonius Wind Turbine: Wind Tunnel Testing and Numerical Simulation. *Journal of Applied Fluid Mechanics* 12(3), 819–829.

Clausen, P. D. and D. H. Wood (1999). Research and development issues for small wind turbines. *Renewable Energy* 16(1-4–4 pt 2), 922–927.

Clausen, P. D. and D. H. Wood (2000). Recent Advances in Small Wind Turbines Technology. *Wind Engineering* 24, 189–201.

EL-Okda, Y. M. (2015). Design Methods of horizontal axis wind turbine rotor blades. *International Journal Industrial Electronics and Dives* 2, 135–150.

Eltayesh, A., F. Castellani, M. Burlando, M. B. Hanna, A. S. Huzayyin, H. M. El-Batsh and M. Becchetti (2021). Experimental and numerical investigation of the effect of blade numer on the aerodynamic performance of a small-scale horizontal axis wind turbine. *Alexandria Engineering Journal* 60, 3931–3944.

Hsiao, F. B., C. J. Bai and W. T. Chong (2013). The Permormance Test of Three Differente Horizontal Axis Wind Turbine HAWT Blade Shapes Using Experimental and Numerical Methods. *Energies* 6, 2784–2803.

Hsu, C. H., J. L. Chen, S. C.Yuan and K. Y. Kung (2021). CFD simulation on the Rotor Dynamics of a Horizontal Axis Wind Turbines Activated from Stationary. *Applied Mechanics* 2, 147–158.

Karthikeyan, N., K. K. Murugavel, S. A. Kumar and S. Rajakumar (2015). Review of aerodynamic developments on small horizontal axis wind turbine blade. *Renewable and Sustainable Energy Reviews* 42, 801–822.

Khalil, Y., L. Tenghiri, F. Abdic and A. Bentamy (2018). Efficiency of a small wind turbine using BEM and CFD. *International Conference on Renewable Energies and Energy Efficiency* 1, 1–10.

Mayer, C., M. E. Bechly, M. Hampsey and D. H. Wood (2001). The starting behavior of a small horizontal axis wind turbine. *Renewable Energy* 22, 411–417.

Pitteloud, J. D. and S. Gsänger (2017). *Small Wind World Report.*

Ramarajan, J. and S. Jayavel (2022). Performance Improvement in Savonius Wind Turbine by Modification of Blade Shape. *Journal of Applied Fluid Mechanics* 15(1), 99–107.

Ryi, J., W. Rhee, U. Hwang and J. S. Choi (2014). Blockage effect correction for a scaled wind turbine rotor by using wind tunnel test data. *Renewable Energy*, 1–9.

Schaffarczyk, A. P. (2014). *Introduction to Wind Turbine Aerodynamics*. Springer.

Shen, X., H. Yang, J. Chen, X. Zhu and Z. Du (2015). Aerodynamic shape optimization and analysis of small wind turbine blades employing the Viterna approach for post-stall region. *Energy Conversion and Management* 119, 266–278.

Singh, R. K. and M. R. Ahmed (2013). Blade design and performance testing of a small wind turbine rotor for low wind speed application. *Renewable Energy* 50, 812–819.

Singh, R. K., M. R. Ahmed, M. Asid zullah and Y. H. Lee (2012). Design of a low Reynolds number airfoil for small horizontal axis wind turbines. *Renewable Energy* 42, 66–76.

Tahani, M. and M. Moradi (2016). Aerodynamic

Investigation of a Wind Turbine using CFD and Modified BEM Methods. *Journal of Applied Fluid Mechanics* 9, 107–111.

Tony Burton David Sharpe, N. J. and E. Bossanyi (2001). *Wind Energy Handbook*. Wiley.

Vardar, A. and I. Alibas (2008). Research on wind turbine rotor models using NACA profiles. *Renewable Energy* 1, 1721–1732.

Wood, D. H. (2001). A blade element estimation of the cut-in wind speed of a small turbine. *Wind Engineering* 25, 125–130.

Wright, A. K. and D. H. Wood (2004). The starting and low wind speed behaviour of a small horizontal axis wind turbine. *Journal of Wind Engineering and Industrial Aerodynamics* 1, 1265–1279.